Studying the influence of the machining process on the geometrical defects of the standardized S-shape test part

Hélène Chanal, E. Duc, A. Chevalier

Studying the influence of the machining process on the geometrical defects of the standardized S-shape test part

Abstract

In 2020, an S-shape part was proposed as a 5-axis reception test part in the new version of ISO 10791-7:2020. This test part enables the testing of machine-tool behavior that involves a high variation in tool axis orientation. This test part is formed of an S-shape fillet which is machined in flank milling with an endmill of Ø20 mm. Any defects of the machined part are influenced by the accuracy of the CAD model, the CAM tool path computation, the measurement uncertainty of the free-formed surface by a coordinate measurement machine (CMM), and machine-tool geometric behavior. This article aims to quantify the influence of all these steps on the final defects of machined parts. The proposed conclusion to our work is based on analytical and numerical study and experimental analysis. Finally, we propose an identification process for machine-tool architecture geometrical defects pertaining to the measurement of the machined S-shape part.

Keywords

S-shape test part, flank milling, five-axis machine-tool accuracy, tool path computation

1 Introduction

Continuous 5-axis machining enables the manufacture of parts with complex shapes and uses a cutting tool deployed across a number of industrial settings, such as mold making or aeronautics. Two machining modes are generally used: end machining with a cylindrical, toroidal, or hemispherical cutter; and flank machining with a cylindrical or conical cutter. The machined parts must meet cost and time requirements while machining a final geometry that conforms to the geometric specifications.

During the execution of a 5-axis machining operation, several classes of defects may influence the machined part [1][2]:

- #1 Geometrical defects due to positions of axes.
- #2 Defects of the guidance of the translation axes (roll, yaw, pitch).
- #3 Inverse transformation defects due to the direct and inverse kinematic models of the machine-tool.
- #4 Errors in the machining path calculation.
- #5 Tool path tracking errors due to the control loop performances of the axes.

- #6 Errors related to the rotation of the cutting tools during machining (spindle runout, tool bending, vibration, etc.).

The influence of thermal defects is not covered in this study.

The geometrical behavior measurement of machine tools is a critical issue, as it influences the geometrical conformity of the machined parts. The purpose of the acceptance or certification of a machine tool is to validate the ability of the machine tool to carry out machining operations in conformity, i.e., with the required accuracy. Several methods can be used to test a machine, depending on the defects to be evaluated:

- Static methods can be used to evaluate defects #1, #2, and #3 using for example lasers, ball bars, or linear scales [3];
- Kinematic methods ensure the evaluation of machine movement accuracy, to quantify, in addition, defect #5 using laser trackers, for example [4];
- Measurement of a machined part ensures an evaluation of the combination of all the defect classes. The machined part can be a test part which is standardized or not. A classical test part for 3-axis machining is introduced in the ISO standard [5].

The problem of defining machine-tool acceptance tests therefore comprises the quantifying of machine-tool accuracy in a configuration close to the future machining configuration. Static and kinematic methods are excellent for setting up machines and evaluating their intrinsic accuracy performance. Generally, they follow requirements defined by a particular standard. However, they do not evaluate the machine-tool behavior during machining; for example, they do not consider the influence of numerical controller behavior in the tool path following defect.

The problem of experimental error evaluation remains complex, and a number of studies are moving toward the implementation of better models for predicting these errors. In this vein, Shneor proposes a piece of software that evaluates the accuracy of a machine-tool for the purpose of 5-axis positional machining [6]. The kinematic model of a machine structure is used to calculate an error matrix. The proposed model can be used to modify a theoretical machining path and deduce the standard errors on the machined surface. The model developed is relatively simple and generic and does not consider the specific kinematic behavior of the machine.

The machining of a part reproduces a machining configuration but induces the appearance of defects #4 and #6. They may affect the quality of the machined part, making this quality a result of factors beyond geometric machine-tool behavior alone. Moreover, further defects can appear as a consequence, for example, of CAD modeling.

The literature proposes different studies for the definition of a test part. For example, Thiebaut defines a particular part for 3 axes free-form machining [7]. Wiessner et al. dedicate part of

their study to the influence of machine-tool thermal deformations [8]. Florussen proposes the use of a torus-shaped test part with a hemispherical tool for evaluating the accuracy of the machine tool during machining [9]. This method can thus assess defects #1 to #5 while minimizing defect #6 because the machining load is reduced. In addition, the surface is geometrically simple to measure. On the other hand, the process is not faithful to the operations generally used on this type of machine tool.

To clarify the reception process, ISO offers a reception part to qualify 5-axis machine tools, introduced in the new version of ISO 10791-7:2020. This test part enables the testing of machine-tool behavior that involves a a high variation in tool axis orientation [10]. This new part is called the S-shape test part. This test part is formed of an S-shape fillet and a rectangular base (Figure 1) [11]. It is machined in flank milling with an endmill of Ø20 mm and generally manufactured from aluminum alloy raw material.

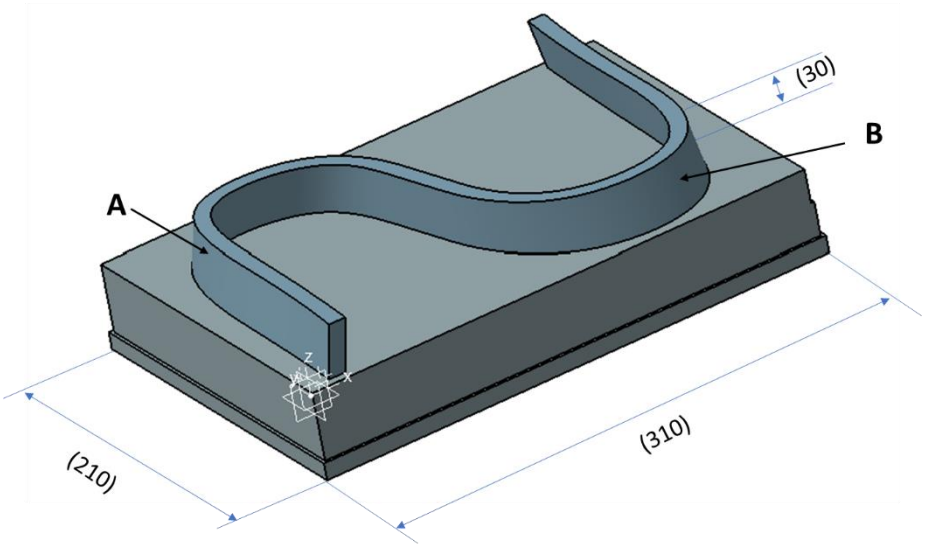

Figure 1: S-shape test part (ISO 10791-7:2020) [5]**.**

A number of recent studies have quantified the dynamic solicitation of each machine-tool axis [12–14]. Su compares the movement of the rotary axes of the NAS 979 test part (first piece defined in the standard to test a 5-axis machine-tool) and the S-shape test part [11]. This comparison shows an increase of the rotary axis acceleration load for the S-shape test part (Figure 2). Thus, this S-shape test part aims to qualify the 5-axis geometrical behavior of a machine-tool and Numerical Controller (NC) behavior.

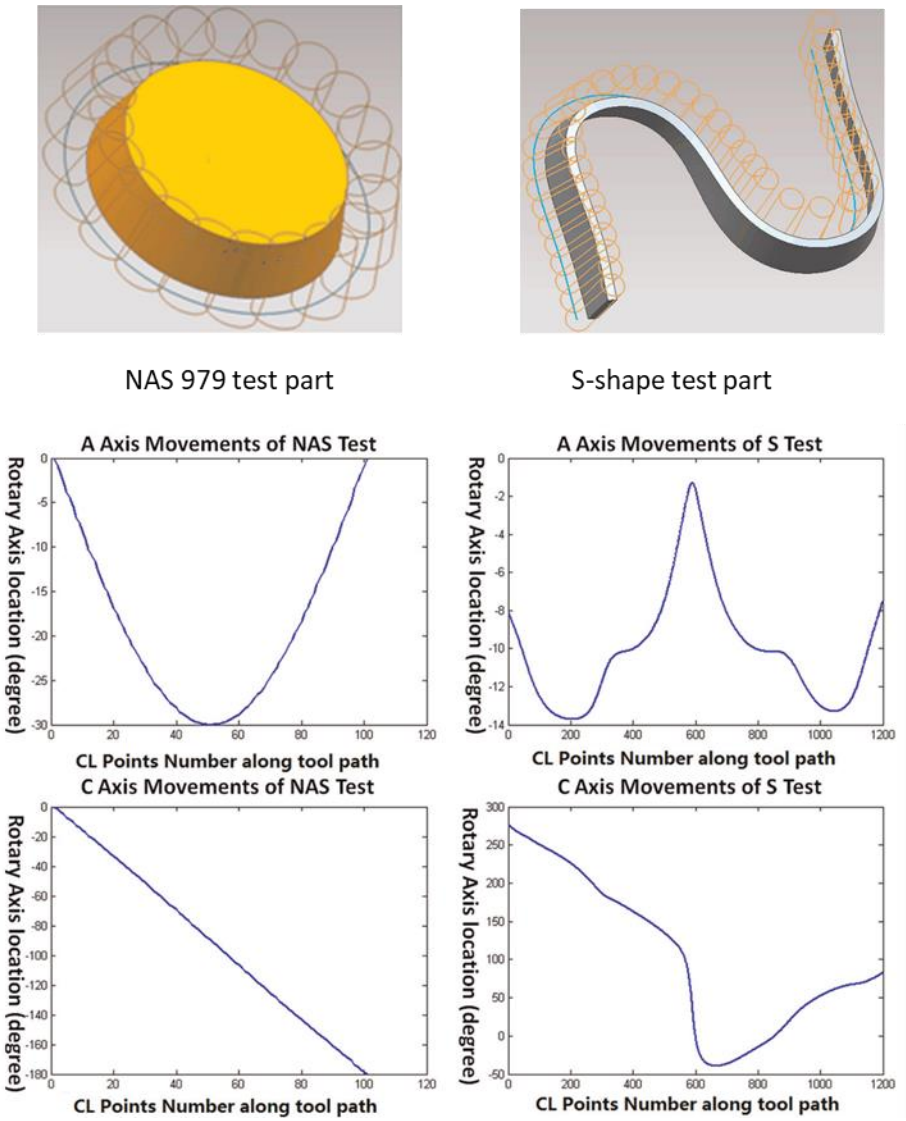

Figure 2: comparison of rotary axes of NAS 979 test piece and S-shape test piece [11]

The fillet is composed of two free-form ruled surfaces A and B defined from fourth-order quasi-uniform rational B-splines (Figure 1). The test result is therefore influenced by the accuracy of the CAD model, the CAM tool path computation, the measurement uncertainty of free form surface by a coordinate measurement machine (CMM), and the machine-tool geometric behavior [15]. Sato's first study investigates the influence of the CAM software and geometrical machine defects on machined S-shape part defects [16]. In Sato's work, the study of CAM software is limited to setting up trajectory computation tolerance.

This paper therefore aims to study the influence of each step of the machining process on the part defect in order to improve the acceptance testing process of machine tools. The idea is to separate all geometrical defects occurring in the machining process including modeling parts, calculating the tool path, and the kinematic behavior of the machine tool. In so doing, by

measuring the machined S-shape test part, we can be sure to identify the behavior that is detrimental to geometric quality.

After an introduction of the S-shape test part, a first analytical study is undertaken in order to identify overcut and undercut resulting from tool path computation. A second study shows the influence of CAM software with an analysis of the tool path computation process. In a third step, the influence of the kinematic behavior of the machine tool is studied. Finally, an S-shape test part is machined, and the measurement results are presented. In the light of both these measurements and the findings of previous studies, we propose correction actions to improve the accuracy of machining of part similar to S-shape test pieces. These correction actions should ensure the improvement of machine-tool accuracy during the 5-axis machining of free-form surfaces.

2 S-shape test part introduction with associated mathematical means

The two fillet surfaces machined in flank milling of the S-shape test part can be analytically described according to the standard model.

In the following, the geometry of the S-shape test part is introduced. Following this, we provide the definitions of the four fourth-order (cubic) quasi-uniform rational B-splines and the two ruled surfaces.

2.1 Geometrical S-shape test part definition

The S-shape test part is composed of two ruled surfaces. Each surface follows two fourth-order quasi-uniform rational B-splines. The table in Figure 3 gives the control point positions for each fourth-order quasi-uniform rational B-spline used to define ruled surfaces A and B, as given in the ISO standard.

a) Control points of ruled surface A

P_i	POS_X	POS_Y	POS_Z
P_0	-131	-95.5	30
P_1	-126	-41	30
P_2	-131	23	30
P_3	-116	78	30
P_4	-51	77	30
P_5	-20	46	30
P_6	-11	10	30
P_7	-9	2	30
P_8	-7	-6	30
P_9	-5	-14	30
P_{10}	3	-46	30
P_{11}	32	-80	30
P_{12}	103	-81	30
P_{13}	116	-13	30
P_{14}	110	43	30
P_{15}	115	99.5	30

Q_i	POS_X	POS_Y	POS_Z
Q_0	-137	-95.5	0
Q_1	-134	-41	0
Q_2	-138	23	0
Q_3	-118	87	0
Q_4	-49	84	0
Q_5	-23	58	0
Q_6	-11	10	0
Q_7	-9	2	0
Q_8	-7	-6	0
Q_9	-5	-14	0
Q_{10}	3	-46	0
Q_{11}	36	-88	0
Q_{12}	111	-84	0
Q_{13}	119	-13	0
Q_{14}	118	43	0
Q_{15}	121	99.5	0

b) Control points of ruled surface B

Mi	POS_X	POS_Y	POS_Z
M_0	-121	-95.5	30
M_1	-117	-29	30
M_2	-121	30	30
M_3	-107	68	30
M_4	-62	67	30
M_5	-31	48	30
M_6	-22	12	30
M_7	-20	4	30
M_8	-18	-4	30
M_9	-16	-12	30
M_{10}	-7	-48	30
M_{11}	26	-88	30
M_{12}	95	-91	30
M_{13}	129	-42	30
M_{14}	118	28	30
M_{15}	125	99.5	30

Ni	POS_X	POS_Y	POS_Z
N_0	-127	-95.5	0
N_1	-124	-29	0
N_2	-128	30	0
N_3	-108	76	0
N_4	-62	74	0
N_5	-33	56	0
N_6	-22	12	0
N_7	-20	4	0
N_8	-18	-4	0
N_9	-16	-12	0
N_{10}	-7	-48	0
N_{11}	30	-95	0
N_{12}	100	-97	0
N_{13}	132	-46	0
N_{14}	127	27	0
N_{15}	131	99.5	0

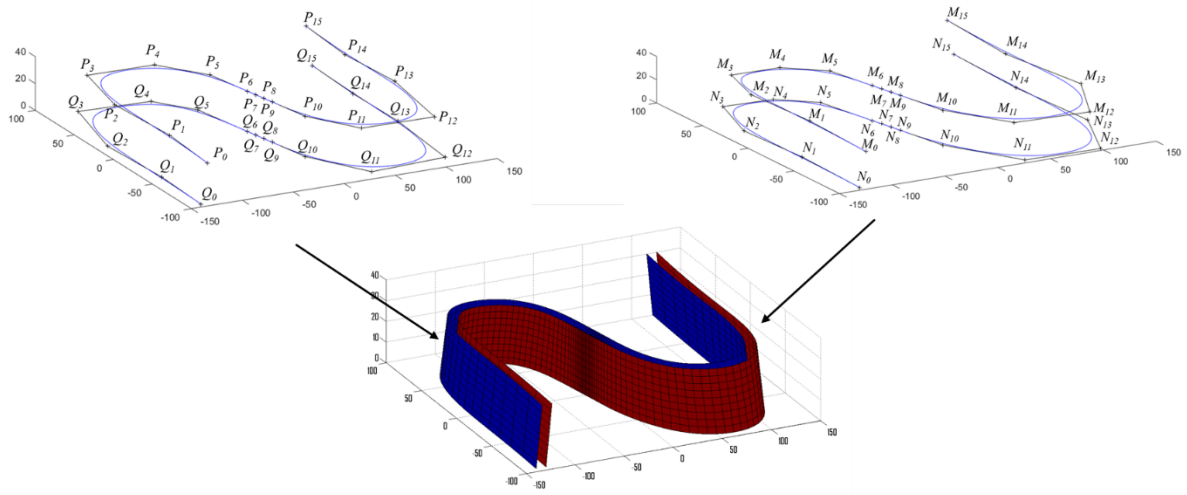

Figure 3: Definition of S-shape part geometry [5]

Each fourth-order quasi-uniform rational B-spline is computed according to the degree m (3 in this case), the set of weighted control points (Figure 3), and the given knot vector. In this case, the knot vector is:

$$U = \left\{0,0,0,0,\frac{1}{13},\frac{2}{13},\frac{3}{13},\frac{4}{13},\frac{5}{13},\frac{6}{13},\frac{7}{13},\frac{8}{13},\frac{9}{13},\frac{10}{13},\frac{11}{13},\frac{12}{13},1,1,1,1\right\}$$
$$= \{u_1, u_2, u_3, u_4, u_5, u_6, u_7, u_8, u_9, u_{10}, u_{11}, u_{12}, u_{13}, u_{14}, u_{15}, u_{16}, u_{17}, u_{18}, u_{19}, u_{20}\}$$

The basic functions $N_{i,m}$ used to compute B-spline equations are then deduced from the recursion formula:

$$N_{i,0}(u) = \begin{cases} 1 \text{ if } u_i \le u \le u_{i+1} \\ 0 \text{ otherwise} \end{cases}$$

And $N_{i,a}(u) = \frac{u-u_i}{u_{i+a}-u_i} N_{i,a-1}(u) + \frac{u_{i+a+1}-u}{u_{i+a+1}-u_{i+1}} N_{i+1,a-1}(u)$ for a = 1 to m with $u\epsilon[u_i, u_{i+1}]$.

Finally, for example, the B-spline curve with P_i control points can be computed from:

$$\mathbf{C_P}(u) = \sum_{i=0}^{n} N_{i,m}(u)\mathbf{P_i} \text{ with } n = 15 \text{ and } u\epsilon[0,1]$$

In the standard, the ruled surface is computed from (Figure 7):

$$\mathbf{S}(u,v) = (1-v) \times \mathbf{C_0}(u) + v \times \mathbf{C_1}(u) \quad (u \in [0,1], v \in [0,1]) \tag{1}$$

Where for surface A, $\mathbf{C_0}(u) = \mathbf{C_Q}(u)$ and $\mathbf{C_1}(u) = \mathbf{C_P}(u)$ and for surface B, $\mathbf{C_0}(u) = \mathbf{C_N}(u)$ and $\mathbf{C_1}(u) = \mathbf{C_M}(u)$.

Thus, the analytical definition of surfaces A and B is computed using equation (1). The machining tool path is derived from these two surfaces. The measurement process of the S-shape test part is described in the ISO standard.

The measurement of the S-shape part is realized in a hundred given points distributed equally on four curves. Two curves are located on surface A and two curves are located on surface B at two different heights 11 mm (named BOTTOM curve) and 25 mm (named TOP curve) (Figure 4).

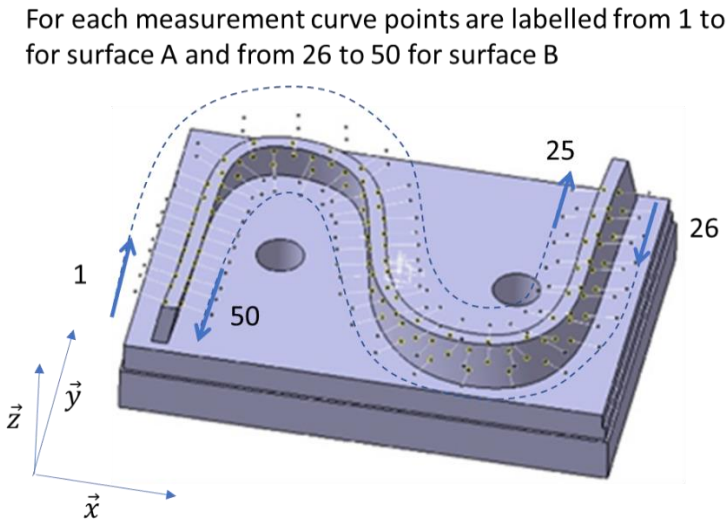

Figure 4: measured points on S-shape test part

In the following, we discuss the impact of the geometrical definition of the S-shape test part on the machining of these surfaces.

2.2 Curve and ruled surface definition in a CAD software

A curve is an application that associates a parameter value to a 3D point. Each S-shape test part surface is defined from an upper curve and a lower curve. Each curve is defined from a fourth-order quasi-uniform rational B-spline. The quasi-uniform knot sequence indicates the structure of the curve setting. This point is particularly critical as it will impact the orientation of the tools and therefore the geometric quality of the machined surface. Traditionally, two types of setting exist: the setting on the curvilinear abscissa (i.e., all along the curve, the parameter is equal to the length ratio from the beginning of the curve, u = 0.5 = middle of the curve) and the quasi-uniform setting.

Mathematically, a ruled surface is calculated by connecting a point on the upper curve to a point on the lower curve which has the same parameter (Figure 7). In CAD software, a ruled surface is constructed by connecting a point on the upper curve to a point on the lower curve. As the two curves are independent, there is not necessarily consistency between the settings of these two curves. Therefore, CAD systems tend to compute point pairs according to a geometric method and not according to the curve setting. The fundamental issue is that curve setting is not always specifiable in CAD software. Thus, the same curve definition can lead to different curve shapes according to the particular CAD software in use.

Figure 5 shows an example of ruled surface computation from the same two curves. The two computed surfaces S1 and S2 are different as the straight line generatrix orientation evolves strongly.

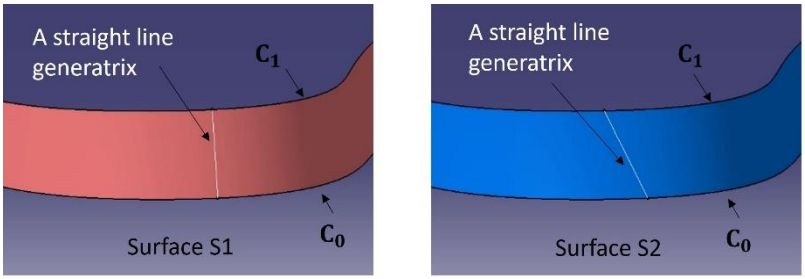

Figure 5: variation of a straight line generatrix according to surface computation method S1 (Left) & S2 (right)

In the context of S-shape test part machining, the exact definition of the surfaces and the deduced orientation of the tool play a key role in the accuracy of the surface model. Indeed, a defect in tool axis orientation leads to a machining defect. To avoid the impact of CAD software, ISO experts choose to attach to ISO 10791-7:2020 a .stp file that defines S-shape part geometry. In the following study, we base our analysis on the analytical definition of the surfaces.

3 Undercut and overcut for non-developable ruled surfaces

A number of studies research tool path computation for non-developable ruled surfaces, particularly in the aeronautical context [17–19]. The main problem of 5-axis flank milling concerns the contact line between the tool and the surface. The presence of a non-zero twist angle makes it impossible to define a machining tool path by the flank allowing the nominal surface to be machined without "overcut" or "undercut" (Figure 6).

3.1 Flank tangent position of a tool on a surface - Undercut and Overcut

The issue of computing the tool position tangent to a surface is complex. The contact is not punctual, but rather as a curve along the tool flank [17]. Only developable ruled surfaces can be machined precisely by a cylindrical or conical tool because the contact curve is equal to a line. Non-developable ruled surfaces lead to interferences between the tool and the part surface which lead to overcut and undercut [19].

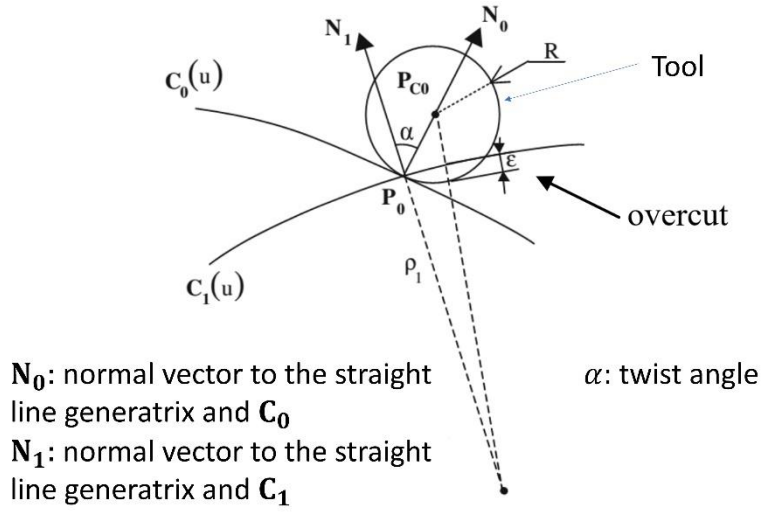

Figure 6: Definition of "overcut" [19]

To quantify overcut and undercut, a first computation of the theoretical tool path is realized with a strict application of equation (1). Several vectors are defined from the S-shape test part (Figure 7):

- $\mathbf{R}(u)$ is a normalized vector as $\mathbf{R}(u) = \frac{\mathbf{C_1}(u) - \mathbf{C_0}(u)}{\|\mathbf{C_1}(u) - \mathbf{C_0}(u)\|}$. $\mathbf{R}(u)$ is along a straight line generatrix of the surface.
- $\mathbf{T}(u,v)$ is the tangent vector of a $\mathbf{S}(u,v)$ curve obtained for a constant v and a variable parameter u. $\mathbf{T}(u,v)$ is therefore perpendicular to $\mathbf{R}(u)$ and can be computed as: $\mathbf{T}(u,v) = \frac{\frac{d\mathbf{S}(u,v)}{du}}{\left\|\frac{d\mathbf{S}(u,v)}{du}\right\|}$ avec $\frac{d\mathbf{S}(u,v)}{du} = (1-v)\frac{d\mathbf{C_0}(u)}{du} + v\frac{d\mathbf{C_1}(u)}{du}$. Note that $\frac{d\mathbf{C_k}(u)}{du} = \sum_{i=0}^{n} \frac{dN_{i,m}(u)}{du}\mathbf{P_i}$.
- $\mathbf{N}(u,v)$ is defined as $\mathbf{N}(u,v) = \pm\mathbf{R}(u) \times \mathbf{T}(u,v)$ to be oriented toward the outside of the part.

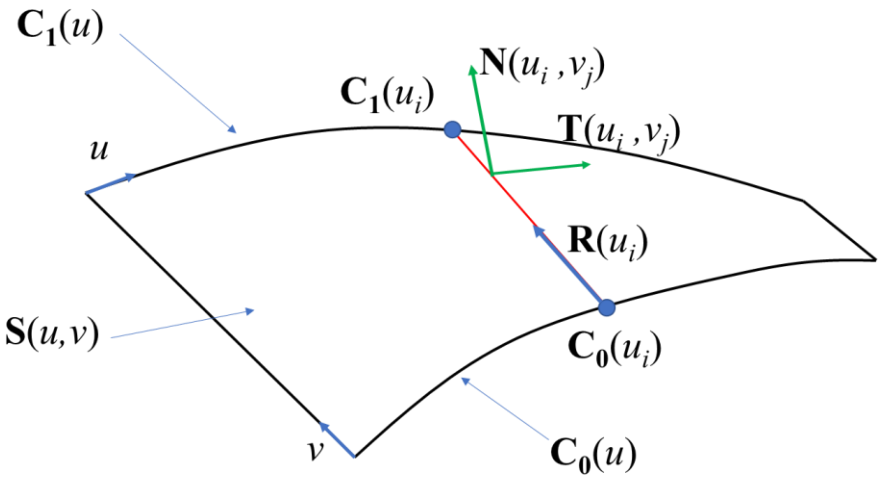

Figure 7: Vector definition to compute analytical tool path

The tool path computation is realized from the assumption that the tool is guided by the curve $\mathbf{C_0}(u)$ and $\mathbf{C_1}(u)$. The axial position of the tool is given by curve $\mathbf{C_1}(u)$ as we consider that the tool section is always in contact with $\mathbf{C_1}(u)$. The tool radius $R_{tool} = 10$ mm and the tool length $L_{tool} = 35$ mm. Thus, the tool path equation is:

$$\mathbf{T_{tool}}(u) = \mathbf{C_1}(u) + R_{tool}\mathbf{N}(u,1) - L_{tool}\mathbf{R}(u) \quad (2)$$

Thus, $\mathbf{R}(u)$ is the tool axis orientation.

The machined surface is the tool envelope surface during the movement along the path [17]. The tool envelope surface can be computed from the property that a point M of the tool belongs to the envelope surface if the normal $\mathbf{n_M}$ to the tool surface at M is perpendicular to the speed of the point M:

$$\mathbf{V}_{M\in tool/0} \cdot \mathbf{n_M} = \mathbf{0} \quad (3)$$

As the tool is cylindrical, $\mathbf{n_M}$ is always perpendicular to the tool axis (Figure 8).

However,

$$\mathbf{V}_{M\in tool/0} = \left(\frac{d\mathbf{OM}}{dt}\right)_0 = \left(\frac{d\mathbf{OE}}{dt}\right)_0 + \mathbf{\Omega} \times (h\mathbf{w} + R_{tool}\mathbf{n}_M) \quad (4)$$

Where O is the center of a fixed coordinate system, E is the tool control point, $\mathbf{OE}$ is the vector from O to E, $\mathbf{\Omega}$ is the instantaneous rotation speed of tool axis as $\mathbf{\Omega} \times \mathbf{w} = \frac{d\mathbf{w}}{dt}$, $\mathbf{w}$ is the unit vector of the tool axis, h is the height of point M and R_{tool} is the tool radius.

In our case study, $\mathbf{OE} = \mathbf{T_{tool}}(u)$ and $\mathbf{w} = \mathbf{R}(u)$.

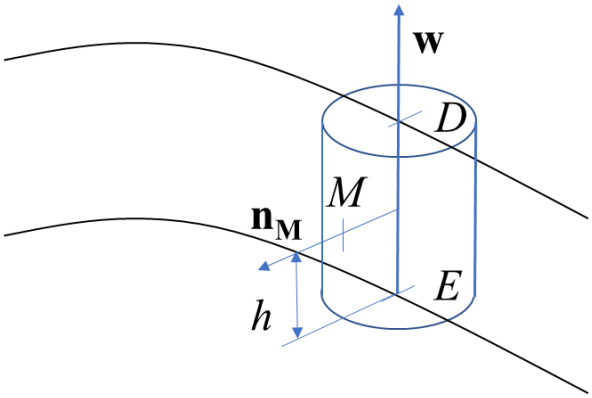

Figure 8: Tool envelope surface computation

Thus, the point M, which belongs to the tool surface envelop, is given by the following equation according to the S-shape test part setting and equation (4):

$$\frac{d\mathbf{T_{tool}}(u)}{du} \cdot \mathbf{n_M} + h\frac{d\mathbf{R}(u)}{du} \cdot \mathbf{n_M} = 0 \quad (5)$$

To solve equation (5), as $\mathbf{n_M}$ is perpendicular to $\mathbf{R}(u)$, it can be written as $\mathbf{n_M}(u,h) = \cos\big(\theta(u,h)\big)\,\mathbf{T}(u,1) + \sin\big(\theta(u,h)\big)\,\mathbf{N}(u,1)$. Thus, a point M belongs to the tool surface envelope if:

$$\tan\big(\theta(u,h)\big) = \pm\frac{\frac{d\mathbf{T_{tool}}(u)}{du}\cdot\mathbf{T}(u,1) + h\frac{d\mathbf{R}(u)}{du}\cdot\mathbf{T}(u,1)}{\frac{d\mathbf{T_{tool}}(u)}{du}\cdot\mathbf{N}(u,1) + h\frac{d\mathbf{R}(u)}{du}\cdot\mathbf{N}(u,1)}$$

Overcut values are then computed from:

$$Overcut(u,h) = R_{tool}\big(1 - \sin\big(\theta(u,h)\big)\big) \quad (6)$$

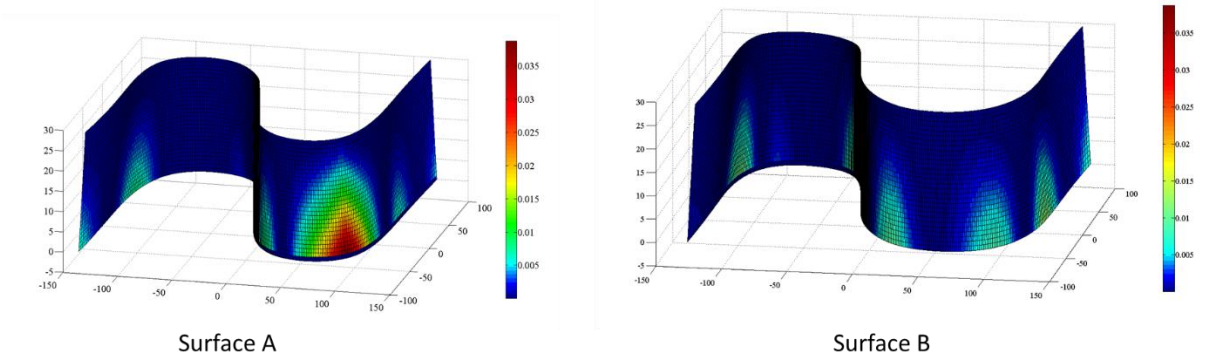

Figure 9: overcut computation for surface A and surface B of S-shape test part

Figure 9 shows the overcut on surface A and surface B (the two sides of the S-shape test part (Figure 3)). A maximum of 0.0387 mm is visualized for surface A and 0.0125 mm for surface B. Such errors should not be blamed on the machine tool. Note that these values are important but lower than the surface profile tolerance of 0.12 mm defined in the standard.

3.2 Influence of the tool radius defect

The tool path is computed from a tool diameter of 20 mm. However, the real tool diameter is not strictly 20 mm. From equation (6), the defect produced on the machined surface due to the tool radius defect can be computed:

$$Def_{tool}(u,h) = (R'_{tool} - R_{tool})\ \sin\big(\theta(u,h)\big)$$

Where R'_{tool} is the real tool radius. Figure 10 illustrates the defect due to a tool radius defect of -0.01 mm. The defect produced on the machined surface is close to the tool radius defect.

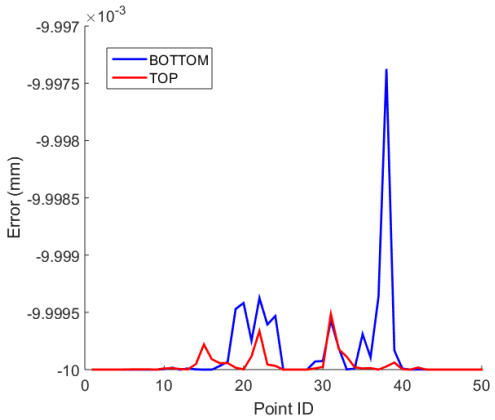

Figure 10: Geometric defect due to a tool radius defect of 0.01 mm

4 Influence of S-part tool path computation

4.1 tool path computation

A number of studies have researched how to modify the tool path to decrease the extent of undercut and overcut [20], [21].

Castagnetti proposes a method of tool path smoothing that can be used in flank milling [22]. A first path is calculated and transformed in the machine coordinate system. For each position, an envelope is also calculated in the machine coordinate system to ensure that tolerances are maintained. Then a new tool path is calculated by minimizing the acceleration variations under the constraints of respecting the envelopes.

The latest methods currently being developed are based on a surface approach that allows tool paths to be smoothed. Path optimization is performed by controlling the distance between the path envelope surface and the surface to be machined. For example, Bo calculates the envelope of a tool of any shape and compares it to the local second-order approximation of the surface to obtain the most favorable directions [23]. The integration of these directions allows tool paths to be calculated.

During machining, adapting the feed rate is also a method of reducing kinematic errors. For example, Chu reduces the errors associated with linear interpolation in the case of flank machining [24]. The author calculates the envelope surface of the tool path and estimates the error induced. He then reduces the feed rate until the error is less than a given tolerance.

These studies involve the implementation of complex computing outside of the CAM environment. However, it is important to propose a method that can be carried out in a CAM environment to allow a large number of manufacturers to achieve this type of test while mastering overcut and undercut without the need for complex numerical computation. In CAM systems, the most robust solution is to calculate the position of the tool tangent to the bottom curve. In a second step, the tool is oriented according to the isoparametric curve or the main direction (Figure 11).

In this case, the straight line generatrix distribution plays a very important role in the occurrence of interference. Indeed, the angle between vectors normal to the surface along the contact line has more or less twist angle which generates more or less interference (Figure 6). In the following figure, the steeply inclined straight line generatrix (surface S2) produces an interference of 0.037 mm, whereas it is zero for surface S1 (Figure 11).

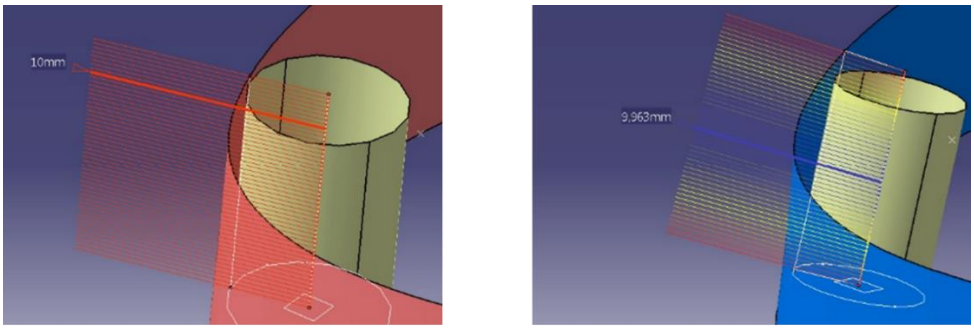

Figure 11: Interference apparition according to the straight line generatrix inclination on surface S1 & S2

In this paper, four part programs are calculated from the original surfaces, using a conventional CAM system, as in an industrial process of machine tool acceptance. The calculation algorithm and the calculation parameters are identical:

- Tool diameter: 20 mm
- Machining tolerance: 0.002 mm
- Distance between points: 0.5 mm

The path calculation algorithm computes the position of the tool tangent to a curve or to both curves and orients the tool according to the isoparametric curve of the tangent surface.

The first program TP1S1 is based on the S1 surface and is computed to be tangential to the top curve to be consistent with the tool path computed in section 3.1. The second TP2S2 is based on the S2 surface which is computed with a different straight line generatrix distribution. For the third program TP3CR, the intersection curves between the surfaces and two planes located at Z11 and Z25 are calculated (Figure 12). These new curves are used to calculate the tangent position of the tool. Note, that these two curves pass through all the measurement points defined in the standard. The tool axis is oriented along the isoparametric curve of the surface. The TP4S1 path is based on surface 1 and the bottom of the part. The tool is oriented along the isoparametric curve of the surface. The contact is located 11 mm from the tool tip along the tool axis.

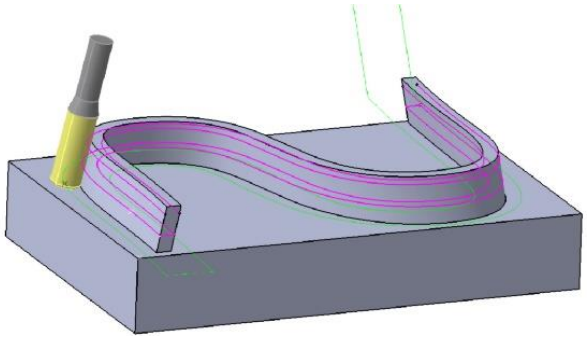

Figure 12: Extracted curves for defining TP3CR

The comparison of the calculated tool paths is based on the calculation of the geometric deviations at the measurement points specified by the standard (Figure 12). For each point P_s, a vector $\mathbf{n_s}$ is computed regarding the normal to the surface. The vector is oriented outwards from the surface and defines a line (n_s). The tool path is discretized with a step less than 0.1 mm. The intersection is calculated between each line (n_s) and each tool position defined by the tool tip and the axis of the tool. The smallest abscissa along the straight line (n_s) of all existing intersections is retained. This calculation follows an opposite approach to the calculation of the envelope area. In Figure 13, the line (n_s) is printed in orange, both intersection points are represented in cyan.

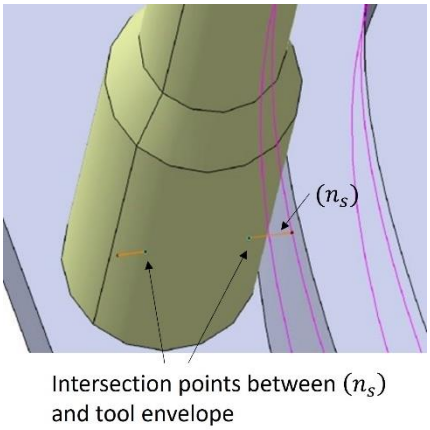

Figure 13: Geometrical deviation calculation

The discretization of the tool path induces an error in the calculation of the geometrical deviation according to equation 7. Equation 7 is the taylor expension of the chord error equation [25]. A discretization $step$ of less than 0.1 mm results in an $error$ of less than 0.000125 mm.

$$error \approx step^2/8R_{tool} \tag{7}$$

The method presents the advantage of being independent of a CAD environment and does not use surface definitions. The error computation is directly linked to the standard points. Then again, estimating deviations can be greater because the distance is computed between two points projected in one direction and not between a point projected on a surface.

Figure 14 presents geometric deviation for the 4 proposed tool paths. Geometrical deviations are computed for the measurement curves. The TOP curve is located at Z25, and the BOTTOM curve is located at Z11. Figure 14 illustrates the position of maximal geometrical deviations on the tool paths TP1S1 and TP2S2. In these figures, all tool positions are merged to illustrate the tool movement.

The computed geometrical deviation for TP1S1 is close to the one computed in Figure 9 as the main difference is the discretization of the TP1S1 tool path. In the case of TP2S2, the

straight line generatrix distribution used to compute the surface S2 is modified which modified the orientation of the tool axis and increase the overcut value (Figure 11). For TP3CR, the use of the two curves which pass through the measurement points allows decreasing the measure of defect due to interference. In the case of TP4S1, the tool path computation is realized to be tangential to a curve close to one of the measure curves, thus the measurement of the defect due to interference decreases too.

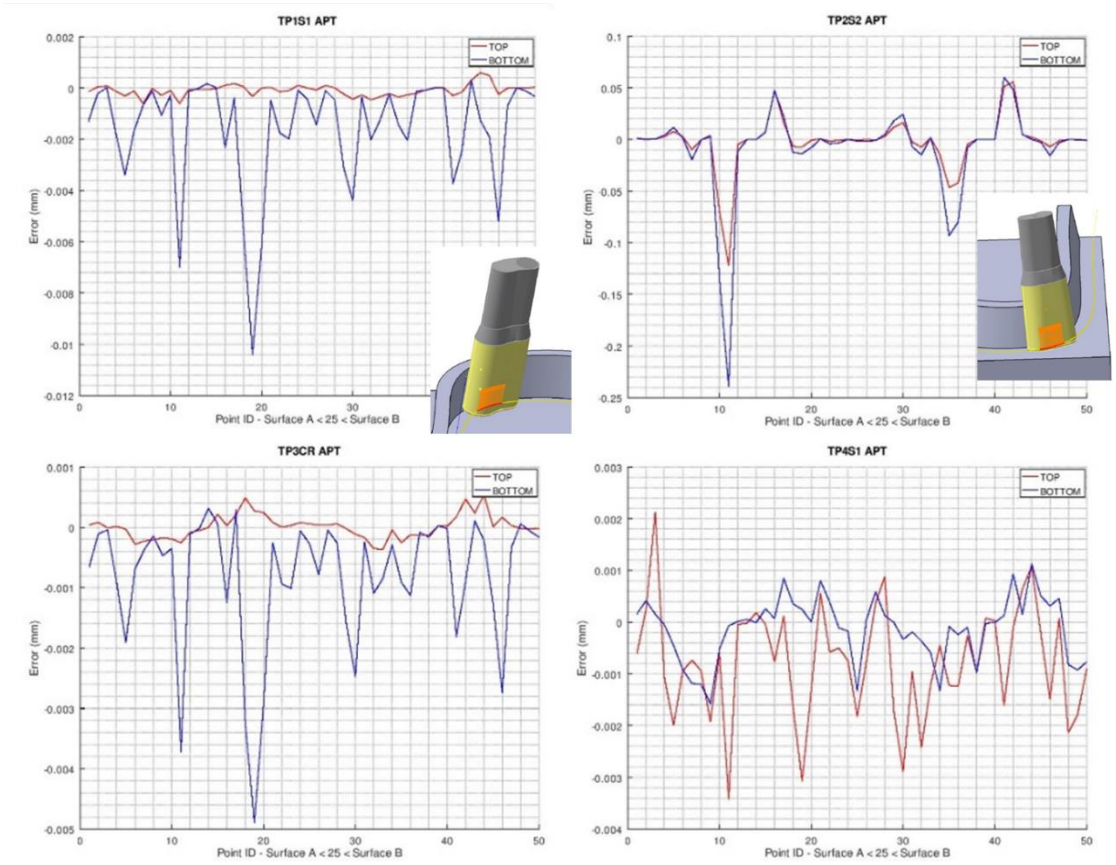

Figure 14: Geometrical deviation results

Despite the tool path accuracy, the geometrical deviations can reach 0.01 mm in the best case, which is an significant value compared to the tolerance expected by the standard (0.12 mm). The TP3CR path, computed from two curves, reduces the value of the geometric deviations to a maximum acceptable value of 0.005 mm.

The analysis shows that in the TP2S2 case, the particular orientation of the isoparametric curve induces very significant errors incompatible with the specifications of the standard. The accuracy of TP4S1 is better than TP1S1 because the computed tool path reduces great variation in tool orientation. Thus, the construction of the surface and the calculation of the tool path play a significant role in the accuracy of the surface. Geometrical deviations affect the quality of the machined surface and it is necessary to separate the errors to identify only machine-related errors.

4.2 B-spline tool path computation

Numerical controls currently offer two interesting features: polynomial interpolation; and space correction of the tool geometry. Thus, it is possible to calculate the tool path without using a CAM system. The problem of calculating the tangent position of the tool and the orientation of the tool axis is directly dealt with by the numerical control without any a priori control.

For the Siemens 840D CNC, using the CUT3DC function gives the program named TP5C1 (Table 1)

```
ORICURVE
      G1    G42
          X-137   Y-95.5     Z0     XH=-131      YH=-95.5       ZH=30
 BSPLINE
    SD=3
          X-134     Y-41     Z0     XH=-126       YH=-41       ZH=30           PL=0
          X-138      Y23     Z0     XH=-131        YH=23       ZH=30     PL=51.4077   ;arc1
          X-118      Y87     Z0     XH=-116        YH=78       ZH=30     PL=51.4077   ;arc2
           X-49      Y84     Z0      XH=-51        YH=77       ZH=30     PL=51.4077   ;arc3
           X-23      Y58     Z0      XH=-20        YH=46       ZH=30     PL=51.4077   ;arc4
           X-11      Y10     Z0      XH=-11        YH=10       ZH=30     PL=51.4077   ;arc5
            X-9       Y2     Z0       XH=-9         YH=2       ZH=30     PL=51.4077   ;arc6
            X-7      Y-6     Z0       XH=-7        YH=-6       ZH=30     PL=51.4077   ;arc7
            X-5     Y-14     Z0       XH=-5       YH=-14       ZH=30     PL=51.4077   ;arc8
             X3     Y-46     Z0        XH=3       YH=-46       ZH=30     PL=51.4077   ;arc9
            X36     Y-88     Z0       XH=32       YH=-80       ZH=30     PL=51.4077  ;arc10
           X111     Y-84     Z0      XH=103       YH=-81       ZH=30     PL=51.4077  ;arc11
           X119     Y-13     Z0      XH=116       YH=-13       ZH=30     PL=51.4077  ;arc12
           X118      Y43     Z0      XH=110        YH=43       ZH=30     PL=51.4077  ;arc13
           X121    Y99.5     Z0      XH=115      YH=99.5       ZH=30           PL=0


ORICURVE
      G1  X-127   Y-95.5     Z0     XH=-121      YH=-95.5       ZH=30
 BSPLINE
    SD=3
          X-124     Y-29     Z0     XH=-117       YH=-29       ZH=30           PL=0
          X-128      Y30     Z0     XH=-121        YH=30       ZH=30     PL=51.2397   ;arc1
          X-108      Y76     Z0     XH=-107        YH=68       ZH=30     PL=51.2397   ;arc2
           X-62      Y74     Z0      XH=-62        YH=67       ZH=30     PL=51.2397   ;arc3
           X-33      Y56     Z0      XH=-31        YH=48       ZH=30     PL=51.2397   ;arc4
           X-22      Y12     Z0      XH=-22        YH=12       ZH=30     PL=51.2397   ;arc5
           X-20       Y4     Z0      XH=-20         YH=4       ZH=30     PL=51.2397   ;arc6
           X-18      Y-4     Z0      XH=-18        YH=-4       ZH=30     PL=51.2397   ;arc7
           X-16     Y-12     Z0      XH=-16       YH=-12       ZH=30     PL=51.2397   ;arc8
            X-7     Y-48     Z0       XH=-7       YH=-48       ZH=30     PL=51.2397   ;arc9
            X30     Y-95     Z0       XH=26       YH=-88       ZH=30     PL=51.2397  ;arc10
           X100     Y-97     Z0       XH=95       YH=-91       ZH=30     PL=51.2397  ;arc11
           X132     Y-46     Z0      XH=129       YH=-42       ZH=30     PL=51.2397  ;arc12
```

```
            X127      Y27     Z0      XH=118         YH=28       ZH=30      PL=51.2397   ;arc13
            X131    Y99.5     Z0      XH=125       YH=99.5       ZH=30           PL=0
```

Table 1: Program TP5C1

It is also possible to calculate mathematically, using equation (1), the equations of the two measurement curves located at Z11 and Z25 (program TP6C2). The equations of these curves are exact and there are no approximations. The program of Table 2 is obtained.

```
ORICURVE
      G1         G42
             X-134.8    Y-95.5      Z11       XH=-132    YH=-95.5    ZH=25
 BSPLINE
    SD=3
           X-131.067      Y-41      Z11   XH=-127.333      YH=-41    ZH=25          PL=0
           X-135.433       Y23      Z11   XH=-132.167       YH=23    ZH=25    PL=51.4077    ;arc1
           X-117.267     Y83.7      Z11   XH=-116.333     YH=79.5    ZH=25    PL=51.4077    ;arc2
            X-49.733   Y81.433      Z11    XH=-50.667   YH=78.167    ZH=25    PL=51.4077    ;arc3
              X-21.9     Y53.6      Z11      XH=-20.5       YH=46    ZH=25    PL=51.4077    ;arc4
                X-11       Y10      Z11        XH=-11       YH=10    ZH=25    PL=51.4077    ;arc5
                 X-9        Y2      Z11         XH=-9        YH=2    ZH=25    PL=51.4077    ;arc6
                 X-7       Y-6      Z11         XH=-7       YH=-6    ZH=25    PL=51.4077    ;arc7
                 X-5      Y-14      Z11         XH=-5      YH=-14    ZH=25    PL=51.4077    ;arc8
                  X3      Y-46      Z11          XH=3      YH=-46    ZH=25    PL=51.4077    ;arc9
            X34.533  Y-85.067      Z11     XH=32.667  YH=-81.333    ZH=25    PL=51.4077   ;arc10
            X108.067    Y-82.9      Z11    XH=104.334    YH=-81.5    ZH=25    PL=51.4077   ;arc11
              X117.9      Y-13      Z11      XH=116.5      YH=-13    ZH=25    PL=51.4077   ;arc12
            X115.067       Y43      Z11    XH=111.333       YH=43    ZH=25    PL=51.4077   ;arc13
              X118.8     Y99.5      Z11        XH=116     YH=99.5    ZH=25          PL=0


ORICURVE
      G1     X-124.8    Y-95.5      Z11       XH=-122    YH=-95.5    ZH=25
 BSPLINE
    SD=3
           X-121.433      Y-29      Z11   XH=-118.167      YH=-29    ZH=25          PL=0
           X-125.433       Y30      Z11   XH=-122.167       YH=30    ZH=25    PL=51.2397    ;arc1
           X-107.633   Y73.067      Z11   XH=-107.167   YH=69.333    ZH=25    PL=51.2397    ;arc2
                X-62   Y71.433      Z11        XH=-62   YH=68.167    ZH=25    PL=51.2397    ;arc3
            X-32.267   Y53.067      Z11    XH=-31.333   YH=49.333    ZH=25    PL=51.2397    ;arc4
                X-22       Y12      Z11        XH=-22       YH=12    ZH=25    PL=51.2397    ;arc5
                X-20        Y4      Z11        XH=-20        YH=4    ZH=25    PL=51.2397    ;arc6
                X-18       Y-4      Z11        XH=-18       YH=-4    ZH=25    PL=51.2397    ;arc7
                X-16      Y-12      Z11        XH=-16      YH=-12    ZH=25    PL=51.2397    ;arc8
                 X-7      Y-48      Z11         XH=-7      YH=-48    ZH=25    PL=51.2397    ;arc9
            X28.533  Y-92.433      Z11     XH=26.667  YH=-89.167    ZH=25    PL=51.2397   ;arc10
            X98.167    Y-94.8      Z11     XH=95.833      YH=-92    ZH=25    PL=51.2397   ;arc11
              X130.9  Y-44.533      Z11      XH=129.5  YH=-42.667    ZH=25    PL=51.2397   ;arc12
              X123.7   Y27.367      Z11      XH=119.5   YH=27.834    ZH=25    PL=51.2397   ;arc13
              X128.8     Y99.5      Z11        XH=126     YH=99.5    ZH=25          PL=0
G1
```

Table 2: Program TP6C2

These two programs present the opportunity to preclude the defect induced by CAM software. To respect the classical numerical chains, we choose to machine and to measure a part with the TP4S1 tool paths.

5 Defect due to machine-tool kinematic behavior

This test part aims to evaluate the behavior of machine-tools during 5-axis machining. It is therefore important to study the impact of the machine-tool on the machining defect regarding CAM tool path computation.

In this section, we begin by assessing the impact of tool path computation realized by the numerical controller. We then discuss the impact of inverse transformation errors.

5.1 Geometrical defect due to numerical controller

The next step concerns the behavior of the machine tool without real machining, i.e., assessing defects due to the numerical controller. The objective is to capture the control tool positions during movements to calculate the associated geometrical deviations. The latest version of the Siemens 840D numerical controller ensures the position of the 5 axes to be captured in the Work Coordinate System (WCS) (i.e., part programming coordinate). The sampling period is 0.008 s. Geometrical deviations are calculated using the same algorithm as in section 4. Figure 15 gives the geometric deviation extract from the numerical controller for the calculated path for the 4 calculated paths. These figures illustrate the geometrical processing of the path performed by the NC manager during tool movement. The processing includes corrections related to the kinematic solicitations, corrections related to the geometrical model of the inverse kinematic transformation according to the selected model.

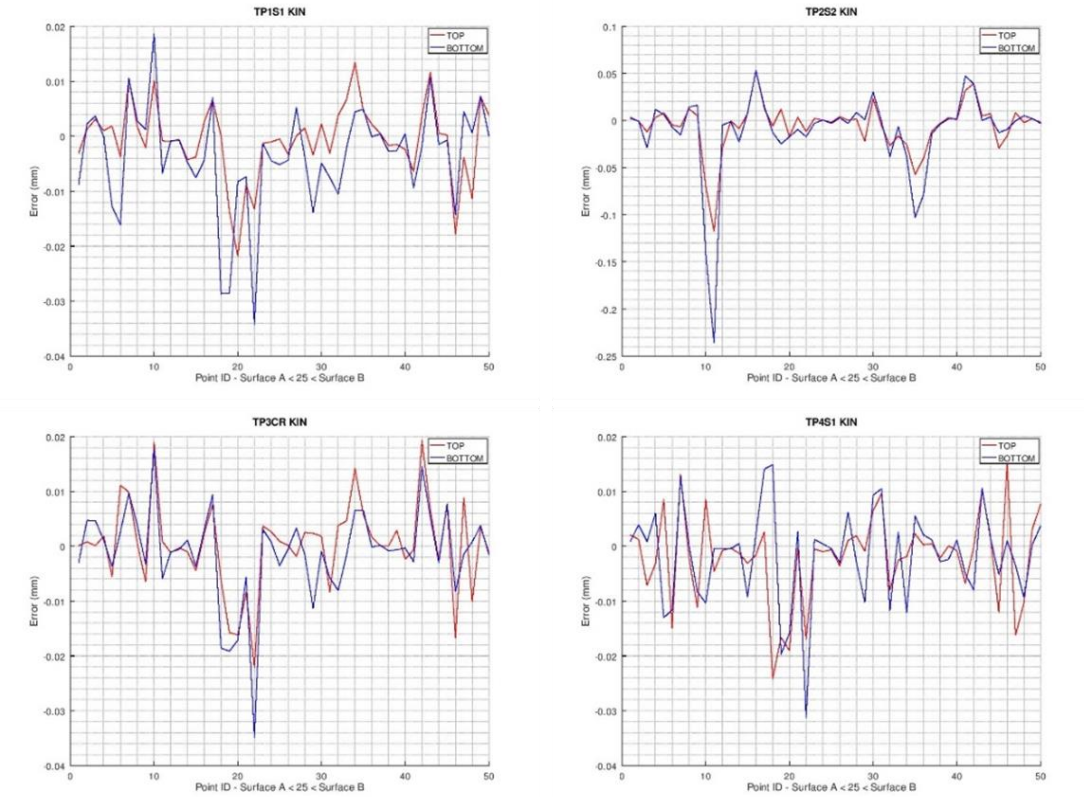

Figure 15: Geometric deviation due to numerical controller

TP1S1, TP3CR, and TP4S1 deviations are very similar. The kinematic behavior of the machine tool is predominant compared to the error profile generated by the tool path. By contrast, in the case of TP2S2, the kinematic error profile is very close to the geometrical error profile. In this case, the error of the tool path calculation is predominant.

The behavior of the machine-tool numerical controller can reach 0.034 mm. It is predominant compared to the error profile generated by the tool path computed by CAM software.

Programs TP5C1 and TP6C2 are also tested. The kinematic behavior of these programs is measured on the machine with the following setting of Cycle 832 (Sinumerik 840D): Ori_Finish, path tolerance = 0.03 mm, angle orientation tolerance = 0.5 degrees (Figure 16).

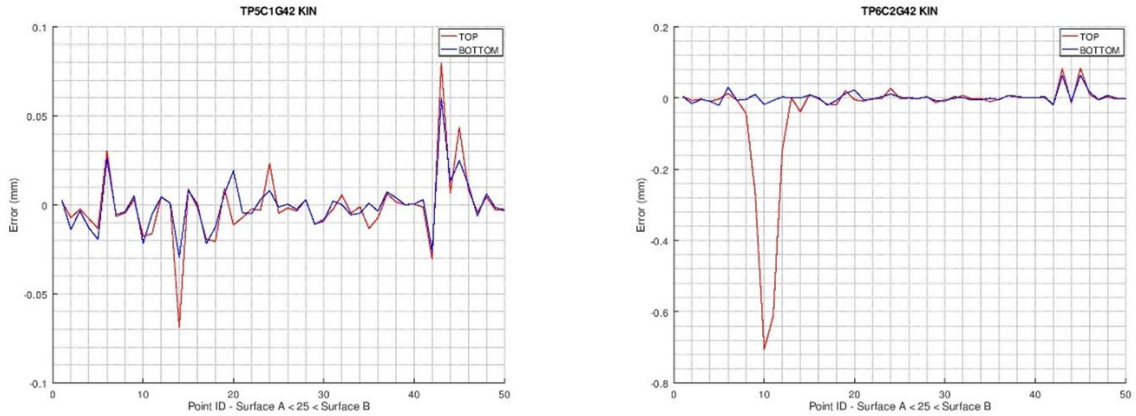

Figure 16: Geometric deviation due to numerical controller for TP5C1 and TP6C2 with the first setting of Cycle 832

A second test is performed on the machine with the following Cycle 832 setting: Ori_Finish, path tolerance = 0.001 mm, angle orientation tolerance = 0.01 degree.

Although the curves describe the S-shape surfaces more accurately, there are significant errors on the tool path following of the TOP curve (at points 14 and 43 for program TP5C1, and at point 10 for program TP6C2). It is therefore a tool orientation error, the calculation of which does not seem to be handled perfectly by the numerical control. Whatever the method used, it is necessary to determine the position and orientation of the tool tangent to the attempted surface. For programs TP5C1 and TP6C2 we cannot control the accuracy of the numerical calculation algorithms realized by the numerical controller.

5.2 Geometrical defect due to inverse transformation errors

Five-axis machine-tools are controlled with a kinematic model. This kinematic model enables the compuatation of the machine-tool tool path regarding attempted tool path in WCS. Thus, errors in this model lead to defects in the machining part. Moreover, this model should be consistent with the machine-tool geometric defect.

In this study, the part is machined on Five Machining Flexiax V. This machine-tool has a rotating table around C-axis and a rotating head around B-axis (Figure 17). (x, y, z) and (i, j, k) are the tool center point and tool axis coordinates in the table coordinate system $(\vec{x}_p, \vec{y}_p, \vec{z}_p)$. (X, Y, Z, B, C) are the axis values. L_0 is the distance between the rotation axis B and the tool center point. $(\vec{x}_T, \vec{y}_T, \vec{z}_T)$ is the tool coordinate system.

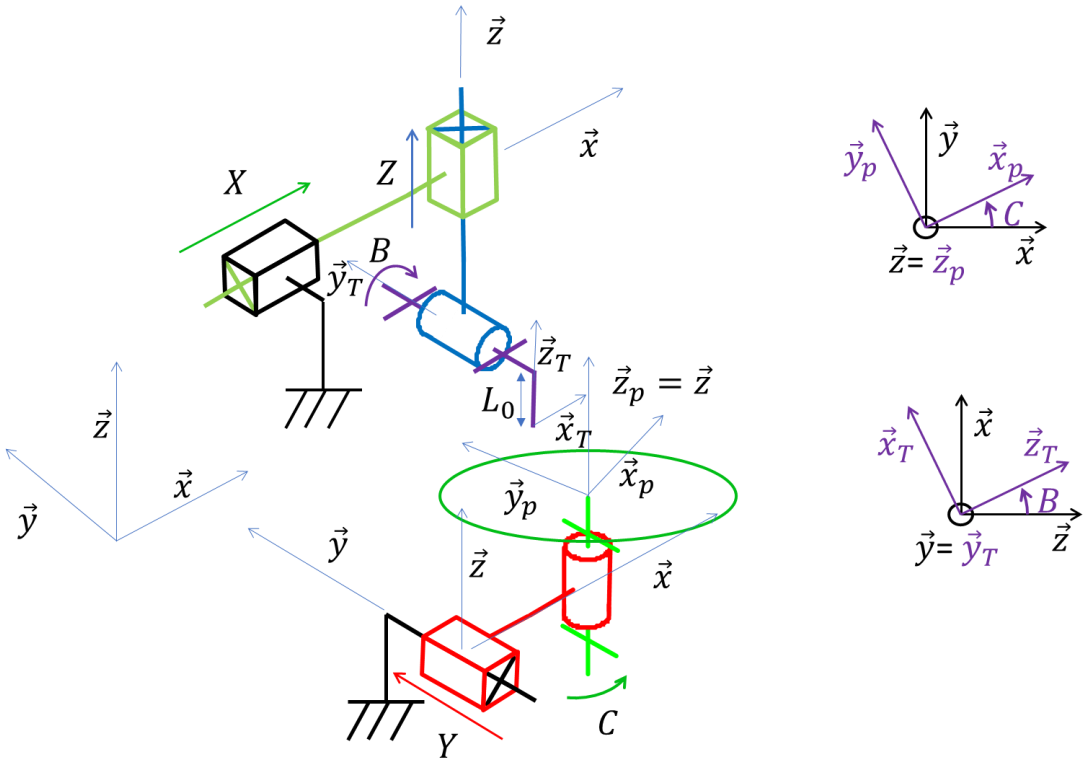

Figure 17: kinematic diagram of machine tool studied

The nominal kinematic model can be computed according to transformation matrices from equation (8) [26].

$$ {}^{O}\mathbf{T}_{X}\,{}^{X}\mathbf{T}_{Z}\,{}^{Z}\mathbf{T}_{B}\,{}^{B}\mathbf{T}_{T}\begin{bmatrix}0\\0\\0\\1\end{bmatrix} = {}^{O}\mathbf{T}_{Y}\,{}^{Y}\mathbf{T}_{C}\begin{bmatrix}x\\y\\z\\1\end{bmatrix} \tag{8}$$

Where ${}^{O}\mathbf{T}_{X} = \begin{bmatrix}1&0&0&X\\0&1&0&0\\0&0&1&0\\0&0&0&1\end{bmatrix}$, ${}^{X}\mathbf{T}_{Z} = \begin{bmatrix}1&0&0&0\\0&1&0&0\\0&0&1&Z\\0&0&0&1\end{bmatrix}$, ${}^{Z}\mathbf{T}_{B} = \begin{bmatrix}\cos(B)&0&\sin(B)&0\\0&1&0&0\\-\sin(B)&0&\cos(B)&0\\0&0&0&1\end{bmatrix}$, ${}^{B}\mathbf{T}_{T} = \begin{bmatrix}1&0&0&0\\0&1&0&0\\0&0&1&-L_0\\0&0&0&1\end{bmatrix}$, ${}^{O}\mathbf{T}_{Y} = \begin{bmatrix}1&0&0&0\\0&1&0&-Y\\0&0&1&0\\0&0&0&1\end{bmatrix}$, ${}^{Y}\mathbf{T}_{C} = \begin{bmatrix}\cos(C)&\sin(C)&0&0\\\sin(C)&\cos(C)&0&0\\0&0&1&0\\0&0&0&1\end{bmatrix}$.

Thus, the direct and inverse nominal kinematic models are given by:

$$\begin{cases} x = Xcos(C) + Ysin(C) - L_o\cos(C)\sin(B) \\ y = -Xsin(C) + Ycos(C) + L_0\sin(B)\sin(C) \\ z = Z - L_0\cos(B) \end{cases} \text{and} \begin{cases} X = xcos(C) - ysin(C) + L_o\sin(B) \\ Y = xsin(C) + ycos(C) \\ Z = z + L_0\cos(B) \end{cases} \tag{9}$$

With $\tan(C) = -\frac{j}{i}$ and $\tan(B) = \frac{\sqrt{i^2+j^2}}{k}$.

Thus, the articular nominal tool path necessary to machine the S-shape test part can be computed from equation (9) as:

$$\mathbf{X_{tool}}(\mathbf{u}) = \begin{bmatrix}X_{tool}(u)\\Y_{tool}(u)\\Z_{tool}(u)\end{bmatrix} = \begin{bmatrix}cos(C_{tool}(u))&-\sin(C_{tool}(u))&0\\\sin(C_{tool}(u))&\cos(C_{tool}(u))&0\\0&0&1\end{bmatrix}\mathbf{T_{tool}}(u) + \begin{bmatrix}L_0\sin(B_{tool}(u))\\0\\L_0\cos(B_{tool}(u))\end{bmatrix} \tag{10}$$

With $\tan(C_{tool}(u)) = -\frac{\boldsymbol{R}(u)\cdot\overrightarrow{y_p}}{\boldsymbol{R}(u)\cdot\overrightarrow{x_p}}$ and $\tan(B_{tool}(u)) = \frac{\sqrt{(\boldsymbol{R}(u)\cdot\overrightarrow{x_p})^2+(\boldsymbol{R}(u)\cdot\overrightarrow{y_p})^2}}{\boldsymbol{R}(u)\cdot\overrightarrow{z_p}}$.

In ISO 230-1, several defects are introduced in order to qualify machine-tool geometric accuracy [2]. Errors are of different natures: errors of the zero position of linear and rotary axes, positioning errors along the direction of motion, straightness errors of translation motion, and angular motion errors. In this study, we focus on the geometric errors which are constant regarding tool pose in the machine-tool workspace. Note that these errors can be introduced in the machine-tool geometrical model which can be implemented in its numerical controller.

For each axis, the reference straight line associated with the axis joint is defined by zero position and orientation errors (Figure 18). According to ISO 230-1, if the machine tool coordinate system is chosen with X-axis is the primary axis, Y-axis is the secondary axis, and the machine-tool origin is chosen to be along the C-axis average line at the height (Z coordinate) where the B-axis average line intersects with the ZX plane when all axes are commanded to zero. Then, only 8 parameters would remain to characterize a 5-axis machine-tool (Table 3) [27].

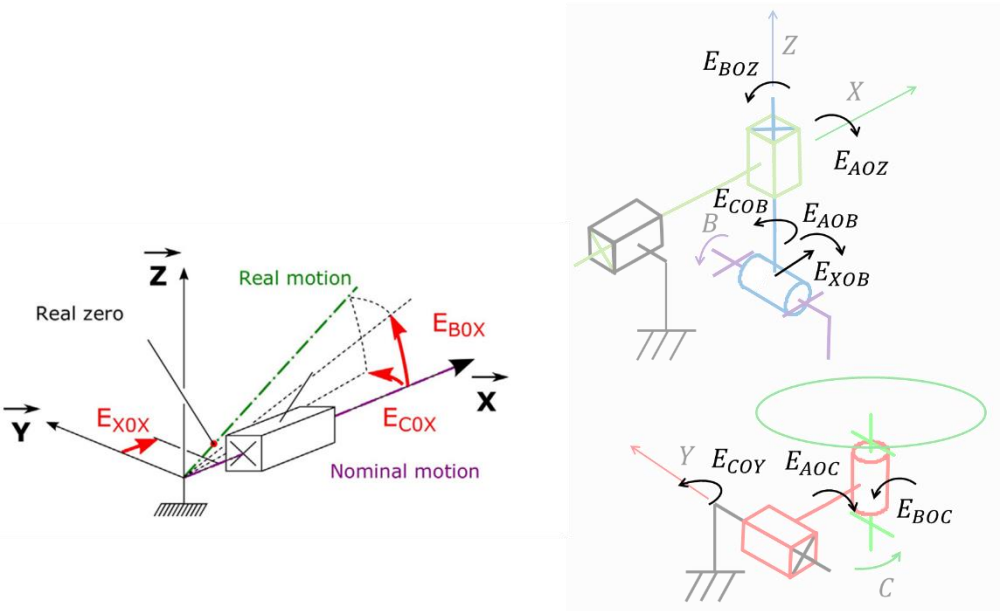

Figure 18: Location and orientation errors of reference straight line for a linear X-axis [28]

	X-axis	Y-axis	Z-axis	C-axis	B-axis
$\boldsymbol{E_{X0i}}$	0	-	-	0	$\boldsymbol{E_{X0B}}$
$\boldsymbol{E_{Y0i}}$	-	0	-	0	-
$\boldsymbol{E_{Z0i}}$	-	-	0	-	0
$\boldsymbol{E_{A0i}}$	-	0	$\boldsymbol{E_{A0Z}}$	$\boldsymbol{E_{A0C}}$	$\boldsymbol{E_{A0B}}$
$\boldsymbol{E_{B0i}}$	0	-	$\boldsymbol{E_{B0Z}}$	$\boldsymbol{E_{B0C}}$	0
$\boldsymbol{E_{C0i}}$	0	$\boldsymbol{E_{C0Y}}$	0	0	$\boldsymbol{E_{C0B}}$

Table 3: Minimum number of error parameters to fully characterize a 5-axis machine tool [2]

In order to develop a geometrical model with these 8 defects, we introduced error transformation matrices into equation (7). These matrices can be written as equation (11), as the error values are small [26]:

$$\mathbf{D_i} = \begin{bmatrix} \sqrt{1 - E_{B0i}^2 - E_{C0i}^2} & -E_{C0i} & E_{B0i} & E_{X0i} \\ E_{C0i} & \sqrt{1 - E_{A0i}^2 - E_{C0i}^2} & -E_{A0i} & E_{Y0i} \\ -E_{B0i} & E_{A0i} & \sqrt{1 - E_{A0i}^2 - E_{B0i}^2} & E_{Z0i} \\ 0 & 0 & 0 & 1 \end{bmatrix}_{R_{i-1}} \quad (11)$$

Where *i* is the studied axis and *i-1* is the previous axis.

Thus, the direct kinematic model with defects can be computed from equation (12).

$$\begin{bmatrix} x \\ y \\ z \\ 1 \end{bmatrix} = DKM(\mathbf{X}, \boldsymbol{\xi}) = \left(\mathbf{D_Y}\ {}^{\mathbf{O}}\mathbf{T_Y}\mathbf{D_C}\ {}^{\mathbf{Y}}\mathbf{T_C}\right)^{-1}\mathbf{D_X}\ {}^{\mathbf{O}}\mathbf{T_X}\mathbf{D_Z}\ {}^{\mathbf{X}}\mathbf{T_Z}\mathbf{D_B}\ {}^{\mathbf{Z}}\mathbf{T_B}\ {}^{\mathbf{B}}\mathbf{T_T}\begin{bmatrix} 0 \\ 0 \\ 0 \\ 1 \end{bmatrix} \quad (12)$$

Where $\mathbf{X} = (X, Y, Z, B, C)^t$ and $\boldsymbol{\xi} = (E_{C0Y}, E_{A0Z}, E_{B0Z}, E_{A0C}, E_{B0C}, E_{X0B}, E_{A0B}, E_{C0B})^t$.

Finally, the induced tool position defect can be computed from a sensitivity analysis with differentiation and linearization of equation (12) [29]:

$$\begin{bmatrix} dx \\ dy \\ dz \end{bmatrix} = \frac{dDKM(\mathbf{X},\boldsymbol{\xi})}{d\boldsymbol{\xi}}\boldsymbol{\xi} \quad (13)$$

$\frac{dDKM(\mathbf{X},\boldsymbol{\xi})}{d\boldsymbol{\xi}}$ is detailed in Appendix A.

With regard to the machined part, the machined defects are computed by subtracting the tool position defect of each point of the tool path and tool position defect on the origin of WCS (the middle of the table in this case). The machining defect on the S-shape test part is then enumerated using a projection of these errors computed from the tool path $\mathbf{X_{tool}}(u)$ along $\mathbf{N}(u, 1)$.

$$Mdef\ (u) = \left(\frac{dDKM(\mathbf{X_{tool}}(\boldsymbol{u}),\boldsymbol{\xi})}{d\boldsymbol{\xi}} - \frac{dDKM((\mathbf{0},\mathbf{0},\mathbf{0},\mathbf{0},\mathbf{0}),\boldsymbol{\xi})}{d\boldsymbol{\xi}}\right)\boldsymbol{\xi} \cdot \mathbf{N}(u, 1) \quad (14)$$

Figure 19 illustrates the simulated machining defects due to a single defect on $E_{C0Y}, E_{A0Z}, E_{B0Z}, E_{A0C}, E_{B0C}, E_{X0B}, E_{A0B}$ and E_{C0B} at each measurement point. This simulation is conducted with $L_0 = 499.889$ mm, which is consistent with the experimental setup presented in the following section.

These graphs can help to detect machine-tool influent defects according to the machining part measurement. Indeed, the machined defect due to inverse transformation errors is a composition of graphs proposed in (Figure 19). However, from the measure of an S-shape test part, defect E_{A0Z} and E_{A0C} cannot be identified separately as their influence on the machined defect is similar except for the sign. This is the same conclusion for defect E_{B0Z} and E_{B0C}.

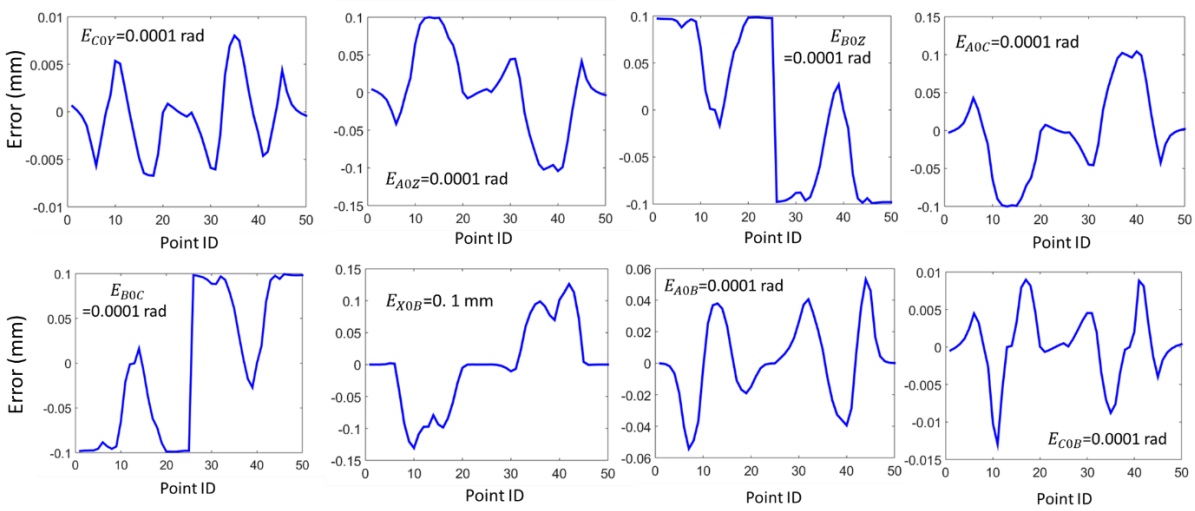

Figure 19: machining defect induced by a single defect on table position

As a final step in our our study, an S-shape test part was machined in Five Machining Flexiax V with program TP4S1.

6 S-shape test part machining and measurement

The S-shape test part is machined in an aluminum alloy according to the standard recommendation with the program TP4S1. For this program, the geometrical deviation due to tool path computation is between [-0.0034 mm; 0.0021 mm] (Figure 14), and the geometrical defect due to numerical controller is between [-0.031 mm; 0.015 mm] (Figure 15).

After machining, the S-shape test part is measured. The measurement process consists of measuring the hundred points defined in the standard (Figure 4). This measure is realized using a CMM (Figure 20). The CMM model is a Trimesure with a maximum permissible error of length measurement $MPEE = \pm\left(3 + \frac{L}{75}\right)$ µm with L in mm and a maximum permissible limit of the repeatability range $R_{0,MPL} = 3$ µm (ISO 10360-2 : 2010).

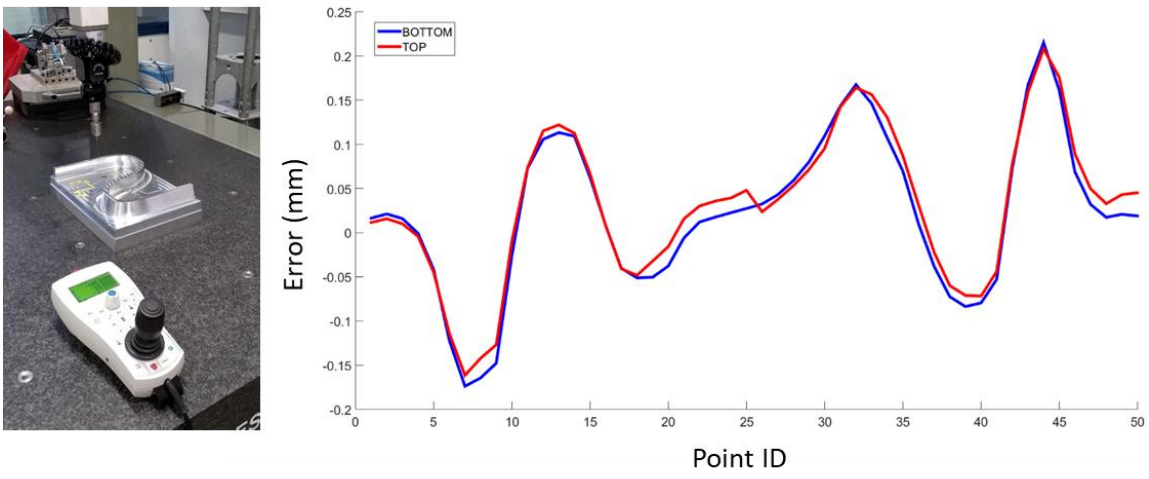

Figure 20: measurement of S-shape test part

As Figure 20 illustrates, the measurement shows that the defects on the top and bottom curves are similar. Thus, the machined defect may be principally due to a tool position defect. The defect measures between -0.18 mm and 0.21 mm which is, unfortunately, greater than expected by the standard, which is 0.12 mm. Moreover, it is a hundred times greater than the defect due to overcut and undercut. In our case, the influence of this defect can be neglected. The defect due to the NC controller is ten times smaller than the measured defect.

However, a comparison between Figure 19 and Figure 20 shows that the measured defect seems to be caused mostly by E_{A0B}. The shape of the influence curve of a defect about E_{A0B} is similar to the measurement defect curve of the S-shape test part. Moreover, a defect near 0.02 mm appears at point 1 which can be due to a tool radius defect of 0.02 mm.

Thus, we can conclude that the measured defect is mostly due to inverse transformation errors. This conclusion and the size of the obtained defect are consistent with other published research on the subejct [1]. Our aim is therefore to use this measure defect on the S-shape test part to identify the machine tool geometric defects that, when their values are implemented in the numerical controller of the machine-tool, are not consistent with the real machine tool geometric behavior.

Thus, an optimization process is realized with the Matlab® lsqnonlin algorithm and by taking into account a tool radius defect of 0.02 mm. The cost function is the difference between the measurement errors at each point and the simulated error from equation (14). To consider that defect E_{A0Z} and E_{A0C}, and defect E_{B0Z} and E_{B0C} cannot be identified separately from the S-shape test part measurement. Six optimization variables replace the machine-tool error parameters in the geometrical model of equation (12) as $x_1 = E_{AOC} = -E_{AOZ}$, $x_2 = E_{BOC} = -E_{BOZ}$, $x_3 = E_{COY}$, $x_4 = E_{XOB}$, $x_5 = E_{AOB}$ and $x_6 = E_{BOZ}$.

The obtained values are given in Table 4 and are coherent with the previous observation.

Error parameters	Identified values	Values for simulation
$x_1 = E_{AOC} = -E_{AOZ}$	-7.0883.10^{-7} rad	0 rad
$x_2 = E_{BOC} = -E_{BOZ}$	-1.2581.10^{-7} rad	0 rad
$x_3 = E_{COY}$	-1.0654.10^{-5} rad	0 rad
$x_4 = E_{XOB}$	0.0294 mm	0.0294 mm
$x_5 = E_{AOB}$	3.2419.10^{-4} rad	3.2419.10^{-4} rad
$x_6 = E_{BOZ}$.	1.2581.10^{-7} rad	0 rad

Table 4: identified values of machine-tool error parameters from S-shape measurement

Figure 21 shows a comparison between measured defects on each measurement point of the S-shape test part and the simulated defects. The residual errors after the optimization process are less than 0.045 mm which respects the standard requirement. These errors are in the same magnitude order of deviation due to the numerical controller (Figure 15 TP4S1 KIN). The identified values of machine-tool error parameters from the S-shape measurements do not ensure the accurate identification of the geometric behavior of the used machine tool as dynamic behaviors are involved during machining, but it gives a first estimation [30][31]. A static measurement process should further be undertaken in order to identify these influent parameters more accurately.

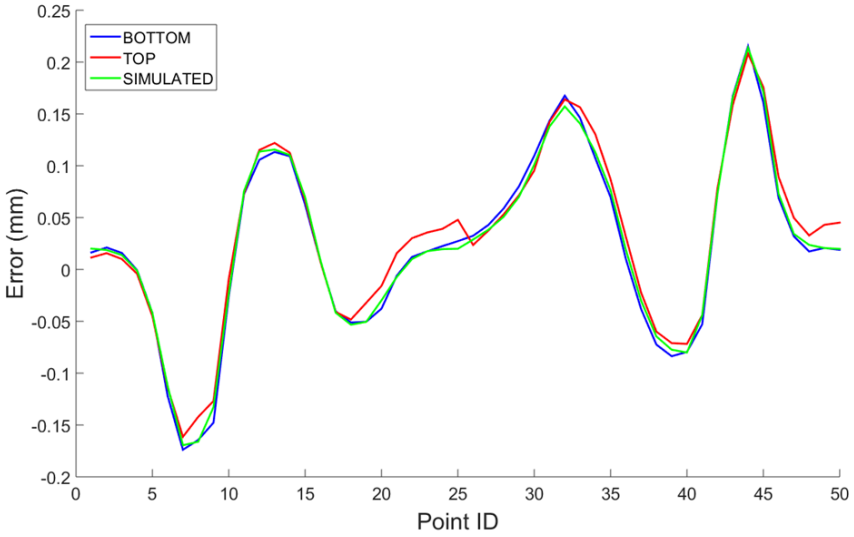

a) Measured defect on the part and simulated defect

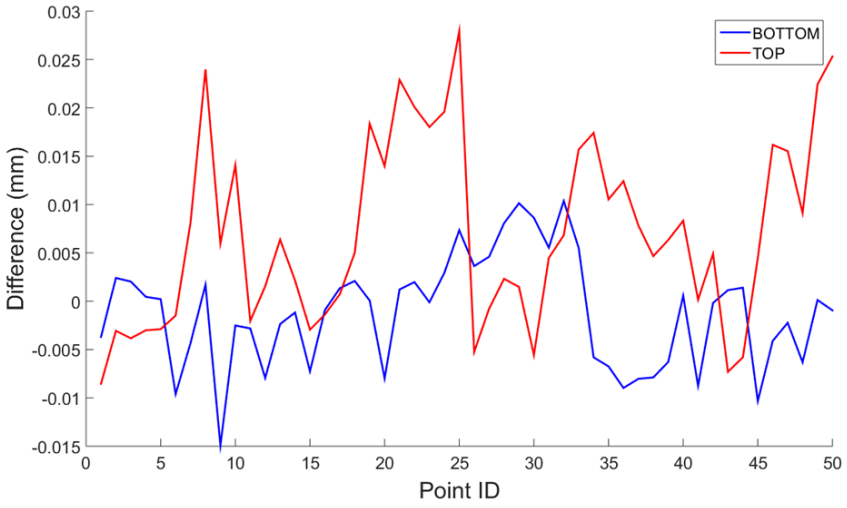

b) Difference between measured defect on the part and simulated defect

Figure 21: identification of machine-tool axis errors from machined defect measurements

To validate this result, a measurement of a gauge block position in WCS is realized for four positions around axis-C with a probe (in this case $L_0 = 533.889$ mm). Measurement results are given in Figure 22. The idea of this test is to measure the same physical points in the table coordinate system using a probe positioned in the machine tool spindle. As the measure is realized in the table coordinate system, we can highlight the inverse transformation error.

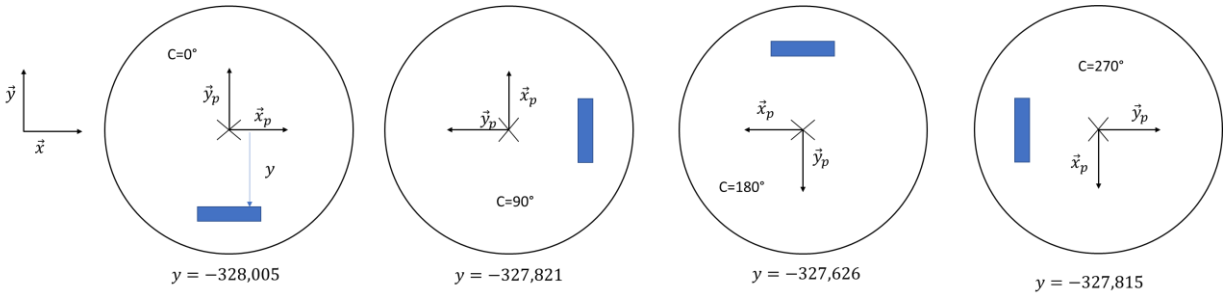

Figure 22: measurement of position defect of the table rotation axis

From equation (12), the machine-tool defect can be identified for each table position measurement:

$$\begin{cases} y_{C=0} = -X_{C=0}E_{C0Y} - (Z_{C=0} - L_0)E_{A0Z} + (Z_{C=0} - L_0)E_{A0C} + L_0E_{A0B} = -328.005 \\ y_{C=90} = -(Z_{C=90} - L_0)E_{B0Z} + (Z_{C=90} - L_0)E_{B0C} - E_{X0B} = -327.821 \\ y_{C=180} = X_{C=180}E_{C0Y} + (Z_{C=180} - L_0)E_{A0Z} - (Z_{C=180} - L_0)E_{A0C} - L_0E_{A0B} = -327.626 \\ y_{C=270} = (Z_{C=270} - L_0)E_{B0Z} - (Z_{C=270} - L_0)E_{B0C} + E_{X0B} = -327.815 \end{cases} \quad (14)$$

However, $X_{C=0} = X_{C=180} = 0$ and $Z_{C=0} = Z_{C=90} = Z_{C=180} = Z_{C=270} \approx L_0$. Thus,

$$y_{C=180} - y_{C=0} = -2L_0E_{A0B} \text{ and } y_{C=270} - y_{C=90} = 2E_{X0B} \quad (15)$$

Finally, from this test, $E_{A0B} = \frac{0.1895}{L_0} = 3.549.10^{-4}$ rad=0.020° and $E_{X0B} = 0.003$ mm.

The error E_{A0B} found with this test is close (less than 8%) to the one found from the optimization based on the measure of the S-shape test part (Table 4). At the same time, the error E_{X0B} is not the same as that derived from the optimization based on the measure of the S-shape test part. However, the measure on the machine-tool studied is not as accurate as of the measurement on a CMM. The machine-tool studied here is reputed to have a linear position accuracy of the Y-axis of the order of a millimeter hundredth. However, an error E_{X0B} of 0.01 mm generates a maximum machined defect of the S-shape test part of 0.015 mm, which is less than expected by the standard (Figure 19).

This test shows the difficulty of estimating machine-tool geometric defects from direct measurement on the machine tool described in ISO 3655:2006 and ISO 8636-1:2000.

Moreover, we realized the measurement of the parallelism of the tool housing axis with C-axis in plan Y-Z on the assumption that this defect might be similar to E_{A0B}. This test is one of the tests proposed in ISO 3655:2006 for testing the accuracy of a machine-tool. The measured defect is 0.010 mm for a length of 300 mm, i.e. an angular defect of $3.333.10^{-5}$ rad. The measured defect is ten times lower than that identified from the measure of the S-shape. Indeed, the measured defect is not E_{A0B}, i.e., the orientation defect of B-axis around X-axis; it is in fact the orientation defect of B-axis around $\vec{x}_p$.

The comparison of tests introduced in ISO 3655:2006 and the defect extracted from the measurement of the S-shape test part illustrates the benefits of the measurements of the S-shape test part in identifying the geometric behavior of a 5-axis machine-tool. Moreover, in the

case of the S-shape test part, rotating axes move during the part machining, thus ensuring a reception process adapted to 5-axis continuous machining.

7 Conclusion

In this paper, we studied the evolution of the geometry of the S-shape test part during each step of machining in order to quantify the associated impact on the final machined part.

As the S-shape test part is defined from two non-developable ruled surfaces, an overcut appears that can reach 0.0387 mm. This is joined by a defect resulting from CAM software tool path computation. The maximum computed deviation is 0.01 mm. The movement of the machine-tool axis is imposed by the numerical controller. This step generates a supplementary maximum deviation of 0.034 mm. Finally, we analyzed the influence of inverse transformation errors resulting from the gap between the geometric model implemented in the numerical controller and the real geometric behavior of the machine-tool studied. Developing a geometric model which integrates error parameters used by the standard to characterize a 5-axis machine tool shows the significant influence of inverse transformation errors in continuous 5-axis machining. Moreover, the sensitivity analysis of the machine-tool geometric parameters on the machined defect of the S-shape test part shows that defect E_{A0Z} and E_{A0C} have a similar influence on the machined defect as for defect $E_{\mathrm{B}0Z}$ and $E_{\mathrm{B}0C}$.

To this day, there is still no standard test for identifying all defects, as some of them are only influent during 5-axis continuous machining. The standard is not yet completely developed for a continuous 5-axis machine-tool.

The use of a geometric model ensures the identification of the defects that had detrimental effects on the quality of the S-shape test part. In this light, future research may benefit from studying the accuracy benefit for 5-axis continuous machining of the implementation of an identified geometric model with defects in the numerical controller.

8 References

[1] S. Pateloup, H. Chanal, E. Duc, Process parameter definition with respect to the behaviour of complex kinematic machine tools, Int. J. Adv. Manuf. Technol. 69 (2013) 1233–1248. https://doi.org/10.1007/s00170-013-5118-3.

[2] ISO 230-1:2012 Test code for machine tools. Geometric accuracy of machines operating under no-load or quasi-static conditions, (2012).

[3] T. Kenno, R. Sato, K. Shirase, S. Natsume, H.A.M. Spaan, Influence of linear-axis error motions on simultaneous three-axis controlled motion accuracy defined in ISO 10791-6, Precis. Eng. 61 (2020) 110–119. https://doi.org/10.1016/j.precisioneng.2019.10.011.

[4] U. Mutilba, E. Gomez-Acedo, A. Sandá, I. Vega, J.A. Yagüe-Fabra, Uncertainty assessment for on-machine tool measurement: An alternative approach to the ISO 15530-3 technical specification, Precis. Eng. 57 (2019) 45–53. https://doi.org/10.1016/j.precisioneng.2019.03.005.

[5] ISO 10791-7:2020 Test conditions for machining centres — Part 7: Accuracy of finished test pieces, (2020).

[6] Y. Shneor, V.S. Chapsky, A. Shapiro, Virtual verification of 5-axis machine tools based on workpiece accuracy analysis: Software tool instead of expensive machining tests, Procedia Manuf. 21 (2018) 228–235. https://doi.org/10.1016/j.promfg.2018.02.115.

[7] F. Thiebaut, C. Lartigue, E. Duc, A certification method for the milling process of free-form surfaces using a test part, Int. J. Prod. Res. 37 (1999) 315–327. https://doi.org/10.1080/002075499191788.

[8] M. Wiessner, P. Blaser, S. Böhl, J. Mayr, W. Knapp, K. Wegener, Thermal test piece for 5-axis machine tools, Precis. Eng. 52 (2018) 407–417. https://doi.org/10.1016/j.precisioneng.2018.01.017.

[9] G.H.J. Florussen, H.A.M. Spaan, T.M. Spaan-Burke, Verifying the accuracy of five-axis machine tool focused on kinematic ISO tests using a torus-shaped test work piece, Procedia Manuf. 14 (2017) 58–65. https://doi.org/10.1016/j.promfg.2017.11.007.

[10] Z. Song, Y. Cui, S-Shape detection test piece and a detection method for detecting the precision of numerical control milling machine, US 8,061,052 B2, 2011.

[11] Z. Su, L. Wang, Latest development of a new standard for the testing of five-axis machine tools using an S-shaped test piece, Proc. Inst. Mech. Eng. Part B J. Eng. Manuf. 229 (2015) 1221–1228. https://doi.org/10.1177/0954405414560780.

[12] W. Wang, Z. Jiang, Q. Li, W. Tao, A new test part to identify performance of five-axis machine tool-Part I: geometrical and kinematic characteristics of S part, Int. J. Adv. Manuf. Technol. 79 (2015) 729–738. https://doi.org/10.1007/s00170-015-6870-3.

[13] W. Wang, Z. Jiang, Q. Li, W. Tao, A new test part to identify performance of five-axis machine tool-Part II validation of S part, Int. J. Adv. Manuf. Technol. 79 (2015) 739–756. https://doi.org/10.1007/s00170-015-6869-9.

[14] Z. Jiang, J. Ding, Z. Song, L. Du, W. Wang, Modeling and simulation of surface morphology abnormality of 'S' test piece machined by five-axis CNC machine tool, Int. J. Adv. Manuf. Technol. 85 (2016) 2745–2759. https://doi.org/10.1007/s00170-015-8079-x.

[15] S. Pateloup, H. Chanal, E. Duc, Process definition of preformed part machining for taking benefit of parallel kinematic machine tool kinematic performances, Int. J. Adv. Manuf. Technol. 58 (2012) 869–883. https://doi.org/10.1007/s00170-011-3453-9.

[16] R. Sato, K. Shirase, Y. Ihara, Influence of NC Program Quality and Geometric Errors of Rotary Axes on S-Shaped Machining Test Accuracy, J. Manuf. Mater. (2018). https://doi.org/10.3390/jmmp2020021.

[17] C. Lartigue, E. Duc, A. Affouard, Tool path deformation in 5-axis flank milling using envelope surface, CAD Comput. Aided Des. 35 (2003) 375–382. https://doi.org/10.1016/S0010-4485(02)00058-1.

[18] P.Y. Pechard, C. Tournier, C. Lartigue, J.P. Lugarini, Geometrical deviations versus smoothness in 5-axis high-speed flank milling, Int. J. Mach. Tools Manuf. 49 (2009) 454–461. https://doi.org/10.1016/j.ijmachtools.2009.01.005.

[19] J. Senatore, F. Monies, W. Rubio, Machining of Complex Sculptured Surfaces, Springer-Verlag London, 2012. https://doi.org/10.1007/978-1-4471-2356-9.

[20] L. Guan, J. Mo, M. Fu, E. Al., An improved positioning method for flank milling of S-shaped test piece., Int J Adv Manuf Technol. 92 (2017) 1349–1364. https://doi.org/https://doi.org/10.1007/s00170-017-0180-x.

[21] H. Tao, J. Fan, C. Wu, R. Pan, An optimized single-point offset method for reducing the theoretical error of S-shaped test piece, Int. J. Adv. Manuf. Technol. (2019). https://doi.org/10.1007/s00170-019-03924-7.

[22] C. Castagnetti, E. Duc, P. Ray, Computer-Aided Design The Domain of Admissible Orientation concept : A new method for five-axis tool path optimisation, 40 (2008) 938–950. https://doi.org/10.1016/j.cad.2008.07.002.

[23] P. Bo, M. Barto, On initialization of milling paths for 5-axis flank CNC machining of free-form surfaces with general milling tools, 71 (2019) 30–42. https://doi.org/10.1016/j.cagd.2019.04.012.

[24] C.H. Chu, W.N. Huang, Y.Y. Hsu, Machining accuracy improvement in five-axis flank milling of ruled surfaces, 48 (2008) 914–921. https://doi.org/10.1016/j.ijmachtools.2007.10.023.

[25] Y. Sun, J. Wang, D. Guo, Guide curve based interpolation scheme of parametric curves for precision CNC machining, Int. J. Mach. Tools Manuf. 46 (2006) 235–242. https://doi.org/10.1016/j.ijmachtools.2005.05.024.

[26] F. Viprey, Modélisation et caractérisation des défauts de structure de machine-outil 5 axes pour la mesure in-process, Université Paris-Saclay, 2016.

[27] Y. Abbaszadeh-Mir, J.R.R. Mayer, G. Cloutier, C. Fortin, Theory and simulation for the identification of the link geometric errors for a five-axis machine tool using a telescoping magnetic ball-bar, Int. J. Prod. Res. 40 (2002) 4781–4797. https://doi.org/10.1080/00207540210164459.

[28] F. Viprey, H. Nouira, S. Lavernhe, C. Tournier, Novel multi-feature bar design for machine tools geometric errors identification, Precis. Eng. 46 (2016) 323–338. https://doi.org/10.1016/j.precisioneng.2016.06.002.

[29] M. Givi, J.R.R. Mayer, Validation of volumetric error compensation for a five-axis machine using surface mismatch producing tests and on-machine touch probing, Int. J. Mach. Tools Manuf. 87 (2014) 89–95. https://doi.org/10.1016/j.ijmachtools.2014.08.001.

[30] H. Chanal, E. Duc, P. Ray, J.Y. Hascoët, A new approach for the geometrical calibration of parallel kinematics machines tools based on the machining of a dedicated part, Int. J. Mach. Tools Manuf. 47 (2007) 1151–1163. https://doi.org/10.1016/j.ijmachtools.2006.09.006.

[31] L. Andolfatto, S. Lavernhe, J.R.R. Mayer, Evaluation of servo, geometric and dynamic error sources on five-axis high-speed machine tool, Int. J. Mach. Tools Manuf. 51 (2011) 787–796. https://doi.org/10.1016/j.ijmachtools.2011.07.002.

9 Appendix A

$$\begin{bmatrix} dx \\ dy \\ dz \end{bmatrix} = \frac{dDKM(\mathbf{X}, \boldsymbol{\xi})}{d\boldsymbol{\xi}} \boldsymbol{\xi}$$

$$\Rightarrow \begin{bmatrix} dx \\ dy \\ dz \end{bmatrix}$$

$$= \begin{bmatrix} (L_0 \sin(B) - X)\sin(C) & -(Z - L_0\cos(B))\sin(C) & (Z - L_0\cos(B))\cos(C) & (Z - L_0\cos(B))\sin(C) & -(Z - L_0\cos(B))\cos(C) & \cos(C) & L_0\cos(B)\sin(C) & -L_0\sin(B)\sin(C) \\ (L_0 \sin(B) - X)\cos(C) & -(Z - L_0\cos(B))\cos(C) & -(Z - L_0\cos(B))\sin(C) & (Z - L_0\cos(B))\cos(C) & (Z - L_0\cos(B))\sin(C) & -\sin(C) & L_0\cos(B)\cos(C) & -L_0\sin(B)\cos(C) \\ 0 & 0 & L_0\sin(B) & -Y & X - L_0\sin(B) & 0 & 0 & 0 \end{bmatrix} \begin{bmatrix} E_{COY} \\ E_{AOZ} \\ E_{BOZ} \\ E_{AOC} \\ E_{BOC} \\ E_{XOB} \\ E_{AOB} \\ E_{COB} \end{bmatrix}$$